Mon. Not. R. Astron. Soc. **000**, 000–000 (0000) Printed 18 September 2013 (MN LATEX style file v2.2)

Broadband monitoring tracing the evolution of the jet and disk in the black hole candidate X-ray binary MAXI J1659−152

A.J. van der Horst[1⋆], P.A. Curran[2], J.C.A. Miller-Jones[2], J.D. Linford[3], J. Gorosabel[4,5,6], D.M. Russell[7,8], A. de Ugarte Postigo[4,9], A.A. Lundgren[10], G.B. Taylor[3], D. Maitra[11], S. Guziy[12], T.M. Belloni[13], C. Kouveliotou[14], P.G. Jonker[15,16,17], A. Kamble[16], Z. Paragi[18], J. Homan[19], E. Kuulkers[20], J. Granot[21], D. Altamirano[1], M.M. Buxton[22], A. Castro-Tirado[4], R.P. Fender[23], M.A. Garrett[24,25], N. Gehrels[26], D.H. Hartmann[27], J.A. Kennea[28], H.A. Krimm[26,29], V. Mangano[30], E. Ramirez-Ruiz[31], P. Romano[30], R.A.M.J. Wijers[1], R. Wijnands[1], Y.J. Yang[1]

[1] *Astronomical Institute, University of Amsterdam, Science Park 904, 1098 XH Amsterdam, The Netherlands*
[2] *International Centre for Radio Astronomy Research − Curtin University, GPO Box U1987, Perth, WA 6845, Australia*
[3] *Department of Physics and Astronomy, University of New Mexico, MSC074220, Albuquerque, NM 87131-0001, USA*
[4] *Instituto de Astrofísica de Andalucía (IAA-CSIC), Glorieta de la Astronomía s/n, 18008, Granada, Spain*
[5] *Unidad Asociada Grupo Ciencia Planetarias UPV/EHU-IAA/CSIC, Departamento de Física Aplicada I, E.T.S. Ingeniería, Universidad del País Vasco UPV/EHU, Alameda de Urquijo s/n, E-48013 Bilbao, Spain*
[6] *Ikerbasque, Basque Foundation for Science, Alameda de Urquijo 36-5, E-48008 Bilbao, Spain*
[7] *Instituto de Astrofísica de Canarias (IAC), Vía Láctea s/n, La Laguna E-38205 S/C de Tenerife, Spain*
[8] *Departamento de Astrofísica, Universidad de La Laguna, La Laguna E-38205 S/C de Tenerife, Spain*
[9] *Dark Cosmology Centre, Niels Bohr Institute, Juliane Maries Vej 30, Copenhagen Ø, D-2100, Denmark*
[10] *Joint ALMA Observatory, Alonso de Córdova 3107, Vitacura - Santiago, Chile*
[11] *Department of Astronomy, University of Michigan, 500 Church Street, Ann Arbor, MI 48109, USA*
[12] *Nikolaev National University, Nikolska 24, Nikolaev, 54030, Ukraine*
[13] *INAF-Osservatorio Astronomico di Brera, Via E. Bianchi 46, I-23807 Merate (LC), Italy*
[14] *Space Science Office, ZP12, NASA/Marshall Space Flight Center, Huntsville, AL 35812, USA*
[15] *SRON, Netherlands Institute for Space Research, Sorbonnelaan 2, 3584CA, Utrecht, The Netherlands*
[16] *Harvard-Smithsonian Center for Astrophysics, 60 Garden Street, Cambridge, MA 02138, USA*
[17] *Department of Astrophysics/IMAPP, Radboud University Nijmegen, P.O. Box 9010, 6500 GL, Nijmegen, The Netherlands*
[18] *Joint Institute for VLBI in Europe, Postbus 2, 7990 AA Dwingeloo, The Netherlands*
[19] *Massachusetts Institute of Technology, Kavli Institute for Astrophysics and Space Research, Cambridge, MA 02139, USA*
[20] *European Space Astronomy Centre (ESA/ESAC), Science Operations Department, 28691 Villanuevadela Cañada (Madrid), Spain*
[21] *Departement of Natural Sciences, The Open University of Israel, P.O. Box 808, Ra'anana 43537, Israel*
[22] *Astronomy Department, Yale University, P.O. Box 208101, New Haven, CT 06520-8101, USA*
[23] *School of Physics and Astronomy, University of Southampton, Southampton, Hampshire SO17 1BJ, UK*
[24] *Netherlands Institute for Radio Astronomy (ASTRON), Postbus 2, 7990 AA Dwingeloo, The Netherlands*
[25] *Leiden Observatory, University of Leiden, Postbus 9513, Leiden 2300 RA, The Netherlands*
[26] *NASA/Goddard Space Flight Center, 8800 Greenbelt Road, Greenbelt, MD 20771, USA*
[27] *Department of Physics and Astronomy, Clemson University, Clemson, SC 29634-0978, USA*
[28] *Department of Astronomy and Astrophysics, Pennsylvania State University, University Park, PA 16802, USA*
[29] *Universities Space Research Association, 10211 Wincopin Circle, Suite 500, Columbia, MD 21044, USA*
[30] *INAF, Istituto di Astrofysica Spaziale e Fisica Cosmica - Palermo, Via U. La Malfa 153, I-90146 Palermo, Italy*
[31] *Department of Astronomy and Astrophysics, University of California, Santa Cruz, CA 95064, USA*

18 September 2013

ABSTRACT

MAXI J1659−152 was discovered on 2010 September 25 as a new X-ray transient, initially identified as a gamma-ray burst, but was later shown to be a new X-ray binary with a black hole as the most likely compact object. Dips in the X-ray light curves have revealed that MAXI J1659−152 is the shortest period black hole candidate identified to date. Here we present the results of a large observing campaign at radio, sub-millimeter, near-infrared (nIR), optical and ultraviolet (UV) wavelengths. We have combined this very rich data set with the available X-ray observations to compile a broadband picture of the evolution of this outburst. We have performed broadband spectral modeling, demonstrating the presence of a spectral break at radio frequencies and a relationship between the radio spectrum and X-ray states. Also, we have determined physical parameters of the accretion disk and put them into context with respect to the other parameters of the binary system. Finally, we have investigated the radio-X-ray and nIR/optical/UV-X-ray correlations up to ∼ 3 years after the outburst onset to examine the link between the jet and the accretion disk, and found that there is no significant jet contribution to the nIR emission when the source is in the soft or intermediate X-ray spectral state, consistent with our detection of the jet break at radio frequencies during these states.

Key words: X-rays: binaries − Stars: individual: MAXI J1659−152

1 INTRODUCTION

Black hole X-ray binaries (BHXBs) are usually discovered as transient sources, with a large outburst in X-rays accompanied by increased emission at ultraviolet (UV), optical, near-infrared (nIR) and radio wavelengths (for a review, see e.g. McClintock & Remillard 2006; Belloni 2010; Fender 2010; Gallo 2010; Gilfanov 2010). These systems spend most of their time in a quiescent state, where the optical/nIR emission is emitted by the companion star or the cool accretion disk. The flux across the electromagnetic spectrum increases by orders of magnitude during outbursts, which are powered by increased accretion onto the black hole and can last weeks to months. The radio emission in these outbursts is ascribed to a relativistic jet, and sometimes these sources are named microquasars by analogy to radio-loud active galactic nuclei (Mirabel et al. 1992).

During an outburst BHXBs go through several canonical X-ray spectral states, following a typical trajectory in the hardness-intensity diagram (HID; e.g. Homan et al. 2001; Homan & Belloni 2005; Belloni 2010). Typically, the source will first become significantly brighter while the spectrum is relatively hard and power-law dominated (hard state), after which the source will become spectrally soft and thermal dominated (soft state); and it eventually dims and evolves back to the hard and then quiescent states. The various spectral states can also be associated with different time variability behavior and the presence of certain types of quasi-periodic oscillations (QPOs; e.g. Wijnands, Homan & van der Klis 1999; Casella, Belloni & Stella 2005; Motta et al. 2011). There are various classifications in the literature for the different states, based on spectral and timing behavior. In this paper we follow Homan & Belloni (2005) and Belloni (2010) in identifying the hard-intermediate state (HIMS) and soft-intermediate state (SIMS) in between the hard and soft states (see McClintock & Remillard 2006, for an alternative classification).

The X-ray emission is thought to be produced in the accretion disk and/or a hot corona above the disk, and the UV, optical and nIR emission is also produced in the accretion disk, either intrinsically (e.g. Shakura & Sunyaev 1973) or by reprocessing of X-rays in that same region (e.g. van Paradijs & McClintock 1994). At nIR to optical wavelengths there may also be a contribution from the jet that dominates the radio emission (e.g. Corbel & Fender 2002; Russell et al. 2006). The latter emission is usually described by a flat spectrum and it is bright during the initial hard state. In some models there is also a contribution from the jet at X-ray frequencies (e.g. Markoff & Nowak 2004). During the transition to the soft state the radio emission is quenched, and in some sources discrete ejecta are launched and their radio emission can be spatially resolved (e.g. Fender, Belloni & Gallo 2004).

On 2010 September 25 a new transient was discovered with the Burst Alert Telescope (BAT) onboard the *Swift* satellite, which was initially identified as a gamma-ray burst (GRB) and named GRB 100925A (Mangano et al. 2010). The source was independently detected as a peculiar hard X-ray emitting source by the Gas Slit Camera (GSC) of the Monitor of All-sky X-ray Image (MAXI) instrument onboard the International Space Station, and was designated as MAXI J1659−152 (Negoro et al. 2010). Soon after its discovery it was realized that this new transient was not a GRB (Kann 2010; Xu 2010), and observations with the X-shooter spectrograph at the ESO Very Large Telescope (VLT) identified the source as an X-ray binary (de Ugarte Postigo et al. 2010a; Kaur et al. 2012). The nature of the source was confirmed by the Rossi X-ray Timing Explorer (*RXTE*), classifying it as a black hole candidate (Kalamkar et al. 2010) based on the identification of its low-frequency QPOs. MAXI J1659−152 evolved through the X-ray hardness-intensity diagram in a manner characteristic of low-mass X-ray binaries, and the presence of type-B and type-C QPOs, and the way in which they evolve during the outburst, have provided evidence for the black hole nature of the compact object (Kalamkar et al. 2011; Muñoz-Darias et al. 2011).

Further observations at X-ray and soft gamma-ray energies with *Swift* (Kennea et al. 2010), *INTEGRAL* (Kuulkers et al. 2010), *RXTE* (e.g. Belloni, Muñoz-Darias & Kuulkers 2010), MAXI and *XMM-Newton*, have shown that there are dips in the light curves recurring at a period of 2.414 ± 0.005 hours (Kuulkers et al. 2013). These have been interpreted as absorption dips at the orbital period of the system, which makes MAXI J1659−152 the shortest period black hole candidate known to date (Kuulkers et al. 2012, 2013; Kennea et al. 2011). For absorption dips to occur, the inclination angle of the accretion disk with respect to the line of sight is relatively well constrained at $\sim 65 - 80^{\circ}$. This allows for an estimate of the binary orbital separation, and mass and radius of the donor star. The binary system appears to be compact (orbital separation of > 1.33 $R_{\odot}$) and the companion is suggested to be an M5 or M2 dwarf star (Kuulkers et al. 2013; Kong 2012).

After the source discovery we initiated a broadband follow-up campaign. Besides many of the aforementioned observations at X-ray and soft gamma-ray energies, we observed the source in various UV, optical and nIR bands, and at sub-millimeter and several radio frequencies. A varying optical source was detected with the *Swift* UltraViolet and Optical Telescope (UVOT; Marshall 2010), and in the R-band with BOOTES-2 and IAC80 (Jelinek et al. 2010), while optical variability on minute timescales was found with the Faulkes Telescope (Russell et al. 2010a). At sub-millimeter wavelengths MAXI J1659−152 was detected with the Atacama Pathfinder EXperiment (APEX; de Ugarte Postigo et al. 2010b), and at radio frequencies with the Westerbork Synthesis Radio Telescope (WSRT; van der Horst et al. 2010a). We followed the evolution of the outburst during various transitions at X-ray (Belloni, Motta & Muñoz-Darias 2010; Shaposhnikov & Yamaoka 2010; Muñoz-Darias et al. 2010) and radio (van der Horst et al. 2010c; Paragi et al. 2010) wavelengths.

Here we present the results of our observing campaign across the electromagnetic spectrum, focusing on the broadband modeling of several epochs for which we have well covered spectral energy distributions (SEDs) including observations at several radio frequencies, and on correlations between the different spectral regimes. In Section 2 we describe all our broadband observations and data analysis, and in Section 3 we present the resulting light curves. Our broad-

band spectral modeling is detailed in Section 4, while we discuss the radio-X-ray and nIR/optical/UV-X-ray correlations in the context of other BHXBs in Section 5. We summarize and conclude in Section 6. All uncertainties in measured quantities and modeling parameters are quoted at the 1σ confidence level.

2 OBSERVATIONS & DATA ANALYSIS

2.1 Radio

We observed MAXI J1659−152 at radio and sub-millimeter frequencies ranging from 610 MHz to 345 GHz, using the WSRT, Karl G. Jansky Very Large Array (VLA), Australia Telescope Compact Array (ATCA), and Giant Metrewave Radio Telescope (GMRT). The results of our radio campaign are given in Table 1, and the upper panel of Figure 1 shows the light curves for four of our radio observing frequencies to illustrate the broadband radio evolution of the outburst.

Very Long Baseline Interferometry (VLBI) observations with the European VLBI Network (EVN) and Very Long Baseline Array (VLBA) are presented in Paragi et al. (2013). Resulting fluxes of these observations are not included here, since the source is resolved in those, but we have included the WSRT synthesis-array fluxes from the two EVN observations.

2.1.1 Very Large Array

We used the VLA to observe MAXI J1659−152 over multiple epochs at 5, 8, 22 and 43 GHz, starting on 2010 September 28 (MJD 55467) and ending on 2010 December 24 (MJD 55554), as detailed in Table 1. The VLA was in the DnC configuration (maximum baseline of 1.9 km) for the observations from 28 September to 2 October, and in the C configuration (maximum baseline of 3.4 km) from 7 October through the end of our observations. We used the new WIDAR correlator with 2 sub-bands and 64 channels per sub-band covering a bandwidth of 128 MHz (i.e., 256 MHz in total). We selected 3C286 for our absolute flux calibrator and used two nearby calibration sources, J1707−1415 and J1658−0739, to apply complex gain calibration. For polarization measurements, we used OQ208 as our leakage calibrator.

We performed all of our calibration and reduction in the Astronomical Image Processing System (AIPS; Wells 1985), using standard procedures for radio frequency interference excision, spectral channel selection, and calibration. For estimating the systematic uncertainties in our measured flux densities, we went by the guidelines outlined in the VLA Calibrator Manual. We added in quadrature systematic uncertainties of 3% (4.9 and 8.5 GHz) and 5% (22 and 43 GHz) of the measured flux densities. As with any new instrument, we experienced some "teething trouble" with the VLA. Our first observing run produced little useful data. We only managed to get time on MAXI J1659−152 but had no time on 3C286 for flux calibration and only 1 scan per band on J1658−0739. We used measurements of J1658−0739 from our second observing run to bootstrap fluxes from the first run. We also missed 3C286 at 8.5 GHz during our observing run on 2010 October 11 (MJD 55480) and had to bootstrap the flux calibration using J1707−1415. These problems resulted in significantly higher uncertainties for these two observations.

We determined the degree of polarization in our 5 and 8 GHz observations in the first two weeks of the outburst. We did not detect any significant polarization in our measurements, with 3σ upper limits varying from 1% to 5% in the first three epochs, and tens of percent in the fourth epoch. At later epochs the polarization limits are less constraining due to the reduced brightness of the source.

2.1.2 Westerbork Synthesis Radio Telescope

We performed observations of MAXI J1659−152 with the WSRT at 1.4, 2.3 and 4.9 GHz, using the Multi Frequency Front Ends (Tan 1991) in combination with the IVC+DZB back end in continuum mode, with a bandwidth of 8x20 MHz at all observing frequencies. Complex gain calibration was performed using the calibrator 3C286 for all observations. The observations were analyzed using the Multichannel Image Reconstruction Image Analysis and Display (MIRIAD; Sault, Teuben & Wright 1995) software package, except for the WSRT data that were obtained during VLBI observations, which were analyzed with AIPS. The flux uncertainties were determined with the MIRIAD task imfit, to which the rms noise in the image around MAXI J1659−152 was added in quadrature.

With the initial discovery of the radio counterpart of MAXI J1659−152 we also reported a high degree of linear polarization in the source (van der Horst et al. 2010a). However, careful re-analysis of this first epoch, and also analysis of the other WSRT epochs at 4.9 GHz, does not show any significant polarization, consistent with the non-detections of polarized emission with the VLA.

2.1.3 Australia Telescope Compact Array

MAXI J1659−152 was observed with the ATCA for 4.5 hours on 2010 September 28 (MJD 55467). We used the Compact Array Broadband Backend (CABB; Wilson et al. 2011) to observe simultaneously in two separate frequency bands, centered at 5.5 and 9.0 GHz. Each frequency band comprised 2048 channels, each of width 1 MHz, for a total observing bandwidth of 2048 MHz. The array was in its H75 configuration, with five closely-spaced antennas within 82 m, and a more distant sixth antenna 4.4 km away.

Data were converted to fits format using the MIRIAD software package, and then read into the Common Astronomy Software Applications (CASA) package for data editing, calibration and imaging. We used PKS 1934−638 as the primary calibrator, and J1733−1304 as the secondary calibrator. One of the central antennas was shadowed during observations of the primary calibrator, so had to be flagged. After editing out bad data and performing external gain calibration, we made a naturally-weighted image of the field containing MAXI J1659−152, using the multi-frequency synthesis algorithm in CASA to accurately deconvolve sources with non-zero spectral slopes. Owing to the large hole in the *uv*-coverage arising from the isolation of the sixth antenna, we only used data from the inner antennas during the imaging process, providing an angular resolution

Table 1. Radio and sub-millimeter observations of MAXI J1659−152, with ΔT the number of days after MJD 55464.0 (the source discovery date). WSRT* indicates WSRT observations taken as part of EVN e-VLBI runs (Paragi et al. 2013). Upper limits are given at the 3σ level.

Epoch (MJD)	ΔT (days)	Obser-vatory	0.61 GHz (mJy)	1.4 GHz (mJy)	2.3 GHz (mJy)	4.9 GHz (mJy)	8.5 GHz (mJy)	22 GHz (mJy)	43 GHz (mJy)	345 GHz (mJy)
55464.96 − 55465.08	1.02	APEX	...	...	...	...	...	...	...	15.8±3.0
55465.59 − 55465.82	1.70	WSRT	...	...	...	5.39±0.05	...	...	...	...
55467.05 − 55467.13	3.09	VLA	...	...	...	10.30±1.03	...	10.00±1.05	...	...
55467.17 − 55467.34	3.25	ATCA	...	...	...	9.76±0.06	11.29±0.06	...	...	...
55467.51 − 55467.83	3.67	WSRT	...	6.95±0.14	6.68±0.08	...	...	...	...	...
55468.05 − 55468.13	4.09	VLA	...	...	...	9.88±0.30	10.03±0.31	11.81±0.71	11.19±0.59	...
55469.63 − 55469.76	5.69	WSRT*	...	...	...	9.77±0.10	...	...	...	...
55470.06 − 55470.15	6.10	VLA	...	...	...	10.29±0.32	9.74±0.30	8.84±0.49	4.84±0.35	...
55471.50 − 55471.82	7.66	WSRT	...	9.02±0.16	9.40±0.08	...	...	...	...	...
55471.98 − 55472.06	8.02	VLA	...	...	...	9.23±0.28	7.55±0.42	7.88±0.42	3.74±0.40	...
55473.58 − 55473.75	9.66	WSRT*	...	...	...	3.65±0.09	...	...	...	...
55473.97 − 55474.06	10.01	APEX	...	...	...	...	...	...	...	10.5±3.2
55475.95 − 55476.07	12.01	APEX	...	...	...	...	...	...	...	<6.0
55476.48 − 55476.80	12.64	WSRT	...	1.15±0.10	1.26±0.06	...	...	...	...	...
55476.96 − 55477.04	13.00	VLA	...	...	...	0.63±0.03	0.59±0.03	0.41±0.07	<0.10	...
55479.90 − 55480.05	15.97	APEX	...	...	...	...	...	...	...	<6.3
55480.97 − 55481.01	16.99	VLA	...	...	...	0.59±0.03	0.65±0.06	...	...	...
55482.98 − 55483.03	19.00	VLA	...	...	...	0.95±0.04	0.88±0.04	...	...	...
55484.46 − 55484.78	20.62	WSRT	...	2.23±0.12	...	2.03±0.06	...	...	...	...
55488.37 − 55488.49	24.43	GMRT	<0.42	...	...	...	...	...	...	...
55488.45 − 55488.77	24.61	WSRT	...	<0.27	<0.23	...	...	...	...	...
55488.99 − 55489.03	25.01	VLA	...	...	...	0.23±0.03	<0.069	<0.25	...	...
55494.31 − 55494.52	30.42	GMRT	<0.15	...	...	...	...	...	...	...
55499.90 − 55499.94	35.92	VLA	...	...	...	<0.072	<0.066	...	...	...
55554.64 − 55554.69	90.66	VLA	...	...	...	0.081±0.016	...	...	...	...

of 65 and 42 arcsec at 5.5 and 9.0 GHz, respectively. However, a comparison with higher-resolution VLA data shows that there were no bright confusing sources within these large beams, so the relatively poor angular resolution should not affect our photometry.

A second observation was made on 2010 October 1 (MJD 55470), with a central frequency of 2.1 GHz. Owing to the RFI affecting the majority of the observing bandwidth, and to the short duration of the observation (1.5 hours), we were unable to use these data to place any accurate constraints on the brightness of the target source.

2.1.4 Giant Metrewave Radio Telescope

GMRT observed the field of MAXI J1659−152 on 2010 October 19 and 25 (MJD 55488 and 55494, respectively) at an observing frequency of 610 MHz. Radio sources 3C286 and J1626−298 were used as flux and phase calibrators, respectively. The flux calibrator was observed for about 15 minutes at the start of the target observations. The phase calibrator and the field of MAXI J1659−152 were then observed alternately for 6 and 45 minutes. The analysis of the observations was carried out using AIPS, and resulted in non-detections at this frequency.

2.2 Sub-millimeter

Continuum observations at 870 μm (i.e., 345 GHz) were carried out using the Large APEX BOlometer CAmera (LABOCA; Siringo et al. 2009) installed on the Atacama Pathfinder EXperiment (APEX; Lundgren et al. 2010). Data were acquired at four epochs under good weather conditions (zenith opacity values ranged from 0.17 to 0.43 at 870 μm). Observations were performed using the wobbler on-off mode and data were reduced using the Bolometer Array (BoA) analysis software. The total on-source integration time of the four epochs was 8.6 hr. The telescope pointing was checked every hour, finding an rms pointing accuracy of 2.1 arcsec. Calibration was performed using observations of the primary calibrators Mars, Uranus and Neptune, as well as the secondary calibrators G10.62, IRAS16293 and G5.89. The absolute flux calibration uncertainty is estimated to be 11%.

2.3 Near-Infrared, Optical & Ultraviolet

The nIR (J- and H-band) observations were performed using the 1.3m telescope (previously the 2MASS southern telescope) at the Cerro Tololo Inter-American Observatory (CTIO), which is currently operated by the Small & Moderate Aperture Research Telescope System (SMARTS) consortium (Subasavage et al. 2010). We observed MAXI J1659−152 with an almost daily cadence between 2010 September 29 (MJD 55468) and October 14 (MJD 55483). The data were recorded by a Rockwell HgCdTe Astronomical Wide Area Infrared Imager. Multiple dithered frames were taken and then flat-fielded, sky subtracted, aligned, and average-combined using an in-house IRAF script. We used two nearby 2MASS stars in the field of MAXI J1659−152 as references. The average magnitudes of these comparison stars were used as a basis for differential photometry with respect to MAXI J1659−152. Additional late-time deep observations in the J-band were carried

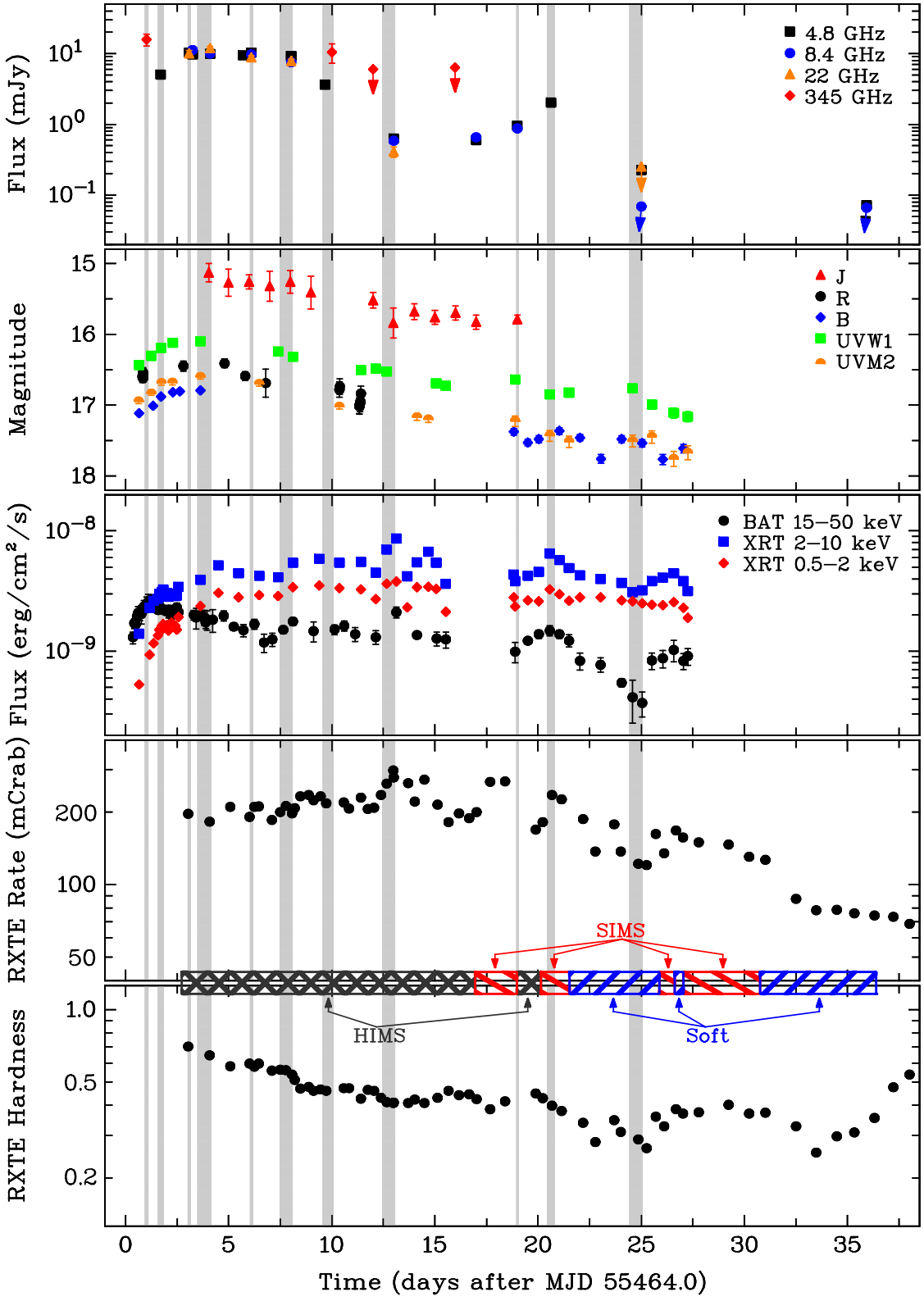

Figure 1. Light curves at various radio and sub-millimeter wavelengths (top panel), in nIR/optical/UV bands (2nd panel from the top), from *Swift*/BAT and *Swift*/XRT (middle panel), and from *RXTE* (2 − 15 keV; 2nd panel from the bottom); and the *RXTE* hardness ratio (6 − 15 keV/2 − 6 keV; bottom panel). The vertical grey bars indicate the epochs for which we performed broadband SED modeling. The times when the source was in the various X-ray states (HIMS, SIMS or soft state) are also indicated (following Muñoz-Darias et al. 2011). Note that the source was in the hard state in the first hours after the outburst onset, but the exact transition from hard state to HIMS is unknown due to the lack of *RXTE* observations.

out with the 3.5m CAHA telescope on 24 July 2013 (MJD 56497) with a total integration time of 38 minutes, resulting in a significant detection of 21.05 ± 0.17 mag, ~ 3 years after the outburst onset.

Optical observations were carried out with the IAC80, 1.23m CAHA, 2.2m CAHA, 2.0m Liverpool, BOOTES-2/Telma and BOOTES-3/Yock-Allen telescopes. The IAC80 telescope is a 0.82m aperture facility, and the observations were done with the CAMELOT camera which is based on a 2k×2k E2V CCD providing a pixel scale of 0.3 arcsec/pixel. The 1.23m CAHA, BOOTES-2/Telma and BOOTES-3/Yock-Allen facilities are Ritchey-Chretien telescopes. The 1.23m CAHA data were acquired with a 2048×2048 SITE#2b CCD which yields a pixel scale of 0.5 arcsec/pixel. Both BOOTES stations are equipped with identical cameras, an Andor iXon-889+ electron multiplying CCD of 1024×1024 pixels, with a pixel scale 0.6 arcsec/pixel (see Castro-Tirado et al. 1999, for more details on the BOOTES network of telescopes). The IAC80 and the 1.23m observations were carried out using standard Johnson/Cousins filters (Fukugita, Shimasaku & Ichikawa 1995), while the images of both BOOTES stations were acquired using Sloan filters (Fukugita et al. 1996).

The 2.0m Liverpool Telescope (LT) observations were made in the SDSS i'-band with RATCam, which yields a pixel scale of $0.135''$/pix based on a 2048x2048 pixel EEV CCD42-40. Additional $g'r'i'z'$-band observations were carried out with the 2.2m Calar Alto telescope equipped with BUSCA. BUSCA is a multichannel camera which allows simultaneous direct imaging in four optical bands using three CCD485 Lockheed Martin plus one CCD485 backside thinned CCD (in the uv channel). The BUSCA observations were done in 2×2 binning and 1k×1k windowing mode, yielding a pixel scale of $0.35\ ''$/pix and a field of view of $6' \times 6'$.

The reduction of all the optical data was performed using standard procedures implemented in IRAF. Calibration of the Sloan data was carried out transforming the Johnson magnitudes of 22 field stars based on Jordi, Grebel & Ammon (2006). The source looks relatively isolated in optical images: there are no entries in either the 2MASS (Skrutskie et al. 1995) or USNO-B1.0 (Monet et al. 2003) catalogues consistent with the position of MAXI J1659−152. Furthermore, observations with the Canada-France-Hawaii Telescope at ~ 18 months after the start of the X-ray outburst result in a quiescent r band magnitude of ~ 23.6 (Kong 2012). We hence assume that the flux at the time of our analysis was dominated by the transient emission of MAXI J1659−152.

Data from the *Swift* UV/Optical Telescope were downloaded from the HEASARC archive and pre-processed at the *Swift* Data Center (see Breeveld et al. 2010), and required only minimum user processing with the *Swift* `FTOOLS` as follows. The image data from each filter, from each observation sequence, were summed using `uvotimsum`. Photometry of the source in individual sequences was derived via `uvotmaghist`, using an extraction region of radius $5''$. `XSPEC` compatible spectral files were created with that same region using `uvot2pha`. The obtained magnitudes are based on the UVOT photometric system (Poole et al. 2008).

In Table 2 we give the results of our ground-based optical follow-up campaign and the *Swift*/UVOT observations.

2.4 X-rays

The outburst of MAXI J1659−152 was observed by several X-ray satellites and instruments. In this paper we focus on the *Swift*, *RXTE* and MAXI observations.

The light curves and spectra of the *Swift* X-Ray Telescope (XRT) were obtained from the XRT online tool, which offers science grade products (Evans et al. 2009). *Swift* Burst Alert Telescope (BAT) data were downloaded from the HEASARC archive and initially processed with the `FTOOL batsurvey`, which applies standard corrections. 8-channel spectra and response files were extracted and the standard spectral systematic error correction applied with `batphasyserr`. All X-ray spectra were binned to have $\geqslant 20$ counts per bin (with `grppha`) so that errors would be approximately Gaussian and hence χ^2 statistics would be valid.

We analyzed all 65 observations of MAXI J1659−152 in the *RXTE* archive. For each observation we extracted a background and dead-time corrected energy spectrum from the PCA standard mode, using only data from Proportional Counter Unit (PCU) 2 of the PCA, as it is the best calibrated and the only one which is always active. We used the standard HEASOFT *RXTE* software to create energy spectra. From these spectra, we extracted background-corrected count rates in the PCA channel bands $A = 0-35$ ($2-15$ keV; total band), $B = 0-13$ ($2-6$ keV; soft band) and $C = 14-35$ ($6-15$ keV; hard band). The *RXTE* rate A, converted to Crab units for PCU 2 (conversion factor of 1 Crab = 2284 counts/second), was used as *RXTE* rate in Figures 1 and 6, while the hardness was defined as the ratio C/B.

The daily count rate ($2-20$ keV) and hardness ($4-10$ keV / $2-4$ keV) as measured by the MAXI instrument have been taken from the MAXI website[1].

3 BROADBAND LIGHT CURVES

Figure 1 shows a broadband overview of the light curves that we obtained in our follow-up campaign of MAXI J1659−152. In this figure we show the light curves at various radio frequencies, nIR, optical and UV bands, and X-ray and soft gamma-ray energies, from the observations presented in Section 2. We do not show light curves in all observing bands to avoid cluttering, but these selected observing bands illustrate the broadband evolution of the MAXI J1659−152 outburst well. For comparison we also show the *RXTE* count rate light curve and hardness evolution, and indicate the times when the source is in the various X-ray states (HIMS, SIMS or soft state), following the identification of these spectral states for MAXI J1659−152 by Muñoz-Darias et al. (2011). We note that the source was only in the hard state during the first hours after outburst onset, before the start of the *RXTE* observations. Because there are no *RXTE* observations during the first two days, we can not identify the exact time of the transition between the hard state and the HIMS.

It can be seen in Figure 1 that the source evolved in different ways in the various parts of the electromagnetic spectrum. In almost all wavebands we witnessed the rise of

[1] http://maxi.riken.jp

the source brightness, except for our APEX sub-millimeter observations which do not have the required temporal sampling, and the nIR observations which started around the peak of the outburst at those wavelengths. The observed trends in the optical, UV and X-ray light curves have been described in Kennea et al. (2011), with a correlated fast rise and slow decay at these frequencies, while the late-time X-ray behavior has been discussed in Homan et al. (2013). At radio frequencies the source was already fairly bright at 1.7 days after the start of the outburst (MJD 55464.0), and reached maximum brightness around day 3. During the following 5 days the radio brightness was constant, after which there was a sudden large decrease of the radio emission (van der Horst et al. 2010c). This radio flux drop was followed several days later by a transition from the hard-intermediate to the soft-intermediate state at X-ray energies (Belloni, Motta & Muñoz-Darias 2010), and the radio flux started rising again after that. Other BHXBs have shown that at the transition to the SIMS, fast radio jets in the form of optically thin, discrete ejecta may emerge. This has, however, not been seen for MAXI J1659−152 (Paragi et al. 2013). After the second rise, the flux dropped significantly again at day 20 after the beginning of the outburst, and subsequently it was only detected at very low flux levels (Miller-Jones et al. 2011; Jonker et al. 2012).

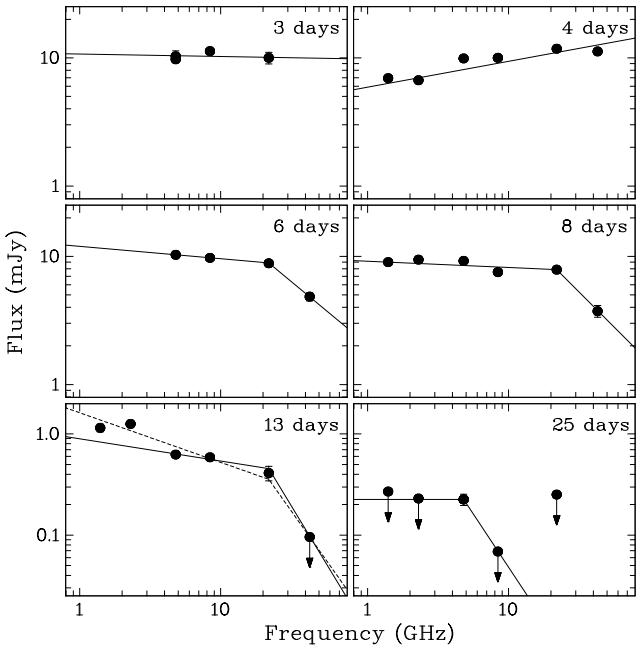

Figure 2. Radio spectra of MAXI J1659−152 for the 6 epochs for which we have at least 3 observing bands. The lines indicate the (broken) power-law fits to the radio spectra. The solid and dashed lines for the spectrum at day 13 show the fits with and without including the low-frequency WSRT data below 3 GHz.

4 BROADBAND SPECTRAL MODELING

Given our rich broadband data set we performed broadband SED modeling. The grey vertical bands in Figure 1 indicate the 11 epochs for which this was done. We made our selection of the epochs based on the times for which we had radio data available. In the X-ray bands we used *Swift*/XRT and *Swift*/BAT data.

The broadband radio-to-X-ray spectra were fit within `XSPEC (12.7.1)`, using χ^2 statistics and accounting for interstellar extinction and absorption, which were modeled by `redden` and `tbabs`, respectively. The observed radio and optical flux densities F_ν at frequency ν, were converted to flux per filter, $F_{\rm filter}$ in units of photons cm^{-2} s^{-1}. This was done via $F_{\rm filter} = 1509.18896 F_\nu\ (\Delta\lambda/\lambda)$, where λ and $\Delta\lambda$ are the effective wavelength and width of respective filters. This flux was then used to produce `XSPEC` compatible files for spectral fitting, using the `FTOOL flx2xsp`.

At all epochs the data were well fit by a phenomenological broken power law at radio frequencies, and by a physically motivated irradiated disk model (`diskir`) at optical/UV and X-ray frequencies (Malzac, Dumont & Mouchet 2005; Gierliński, Done & Page 2008, 2009). In the latter model the X-ray emission consists of thermal emission from the accretion disk and a hard tail caused by Comptonisation of soft seed photons in a hot plasma of energetic electrons. The Comptonised emission in turn illuminates the disk, of which a large fraction gets reflected, but also a significant fraction of the photons are reprocessed and add to the disk emission. The parameters of this model are: the unilluminated disk temperature kT_{disk}; the power-law photon index Γ of the Compton tail; the ratio of luminosity in the Compton tail to that in the unilluminated disk, L_C/L_{disk}; the fraction of bolometric flux which is thermalised in the outer disk, F_{out}; the log of the ratio of outer to inner disk radius, r_{out}; and a normalisation, $Norm$, dependent on the apparent inner disk radius. We note that it has been shown that spectra can be fit by an irradiated disk model even in the hard state (e.g. Miller, Homan & Miniutti 2006; Rykoff et al. 2007).

The χ^2_ν of the fits presented in the next section ranges from 1.1 to 2.0 for $\sim 10^3$ degrees of freedom, which are relatively high but given the disparity of the data (combination of many different instruments, epochs and bands) we deemed those acceptable. Furthermore, any variations from the model show no underlying structure, only noise-like variations.

4.1 Modeling Results

In our modeling the radio emission and the nIR to X-ray emission appear to be due to separate components. Figure 2 shows the radio spectra for 6 of our 11 epochs for which we have at least 3 radio bands. The behavior of the radio SEDs seems more complicated than a single flat or slightly-inverted spectrum across all radio bands (i.e. a spectral index $\sim$ 0). We performed single and/or broken power-law fits to the radio SEDs for the epochs indicated in Figure 1 except for the first two epochs in which there was only one observing frequency. From Figure 2 it can be seen that there are epochs where a single power law is not sufficient to describe the spectrum, which is the case for 4 out of the 9 epochs we fit. For the latter epochs we show both spectral indices in Figure 3, while for the other 5 epochs we only show a single spectral index. In the broken power law fits we fixed the break at 22 GHz for the SEDs at 6, 8 and 13 days after MJD 55464.0, while at 25 days it was fixed at 4.9 GHz. In the former three epochs these break frequen-

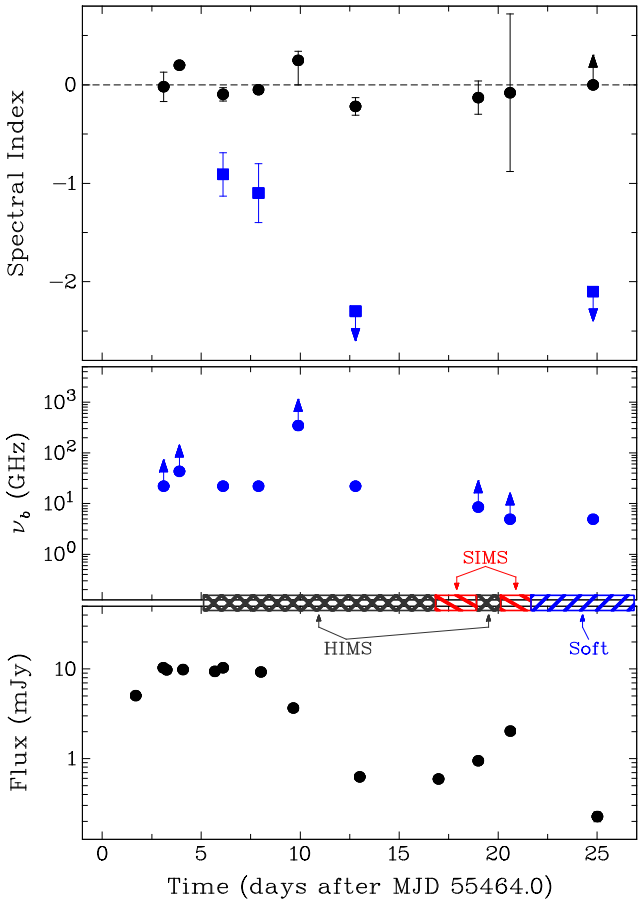

Figure 3. Evolution of parameters from the broken power-law fits to the radio SEDs indicated in Figure 1 except for the first two epochs. The top panel shows the spectral index, with the black circles indicating the low frequency power-law slopes, and the blue squares the high frequencies in those epochs that are best described by a broken power law. The middle panel shows the evolution of the spectral break for all epochs, including those for which we can only put upper or lower limits. In the lower panel the 4.9 GHz light curve and the X-ray spectral states are displayed for comparison purposes.

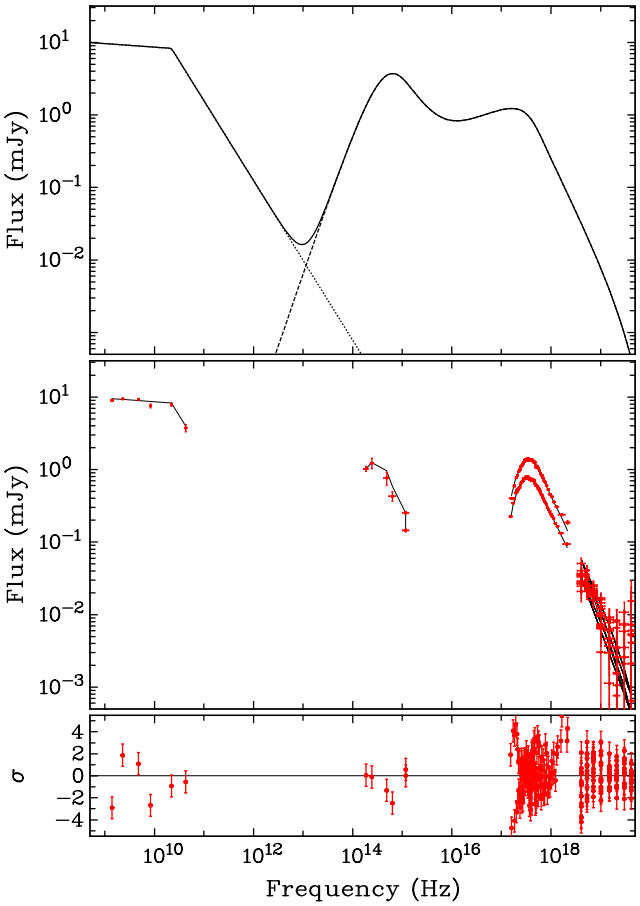

Figure 4. Example model plots for the broadband SED at day 8 after the outburst onset. The top panel shows the spectrum of the best fit model for this particular epoch, with the dotted line showing the broken power-law fit to the radio data, the dashed line the irradiated disk model fit, and the solid line the total spectrum. The middle panel shows the fit of the unfolded spectrum, with the data in red symbols and the best fit model in black lines. In the bottom panel we show the deviations from the best fit model.

cies were fixed because the spectrum is consistent with a single power law up to 22 GHz and there is only one data point at 43 GHz to constrain the break, which makes the parameters of a free broken power-law fit hard to constrain. In fact, the break could be at any frequency in between 22 and 43 GHz and thus the high-frequency spectral indices can be steeper that the ones plotted in Figure 3. At day 25 there is only one detection at 4.9 GHz, hence the lower limit on the low-frequency spectral index and the upper limit on the high-frequency spectral index. We would like to point out, however, that the observations are not strictly simultaneous, so the 4.9 GHz detection could be a short flare with a timescale of hours. For those epochs where a break is not required at radio frequencies, we show lower limits on the break frequency in Figure 3. In our broadband radio-to-X-ray fits we placed those breaks arbitrarily at 10^{-5} keV ($\approx 2.4 \times 10^{12}$Hz), with a steep cut-off.

An example fit to one of the epochs and the broadband model used here are shown in Figure 4. $E(B-V)$ displays no significant variability with an average of 0.595 ± 0.008, consistent with the Galactic value of $E(B-V) = 0.599$ (Schlegel, Finkbeiner & Davis 1998). This is significantly larger than the value of $E(B-V) \simeq 0.35$ derived by Kaur et al. (2012). The measured values of interstellar absorption are consistent with being constant with an average of $N_{\rm H} = (0.319 \pm 0.009) \times 10^{22}\,{\rm cm}^{-2}$. This value is greater than the expected Galactic absorption of $N_{\rm H} = 0.17 \times 10^{22}\,{\rm cm}^{-2}$ (Kalberla et al. 2005) but less than that obtained by Kennea et al. (2011). It should be noted, however, that Kennea et al. (2011) fit a different model and only to the X-ray data, while we include nIR/optical/UV data which add additional constraints to the thermal emission.

Figure 5 shows the evolution of the well-constrained parameters of the irradiated disk model. Although the fit parameter values we obtain are slightly different than the ones from Kennea et al. (2011) and Yamaoka et al. (2012), the trends in their evolution are similar. The disk temperature, kT_{disk}, rises from an initial temperature of 0.13 keV to a relatively stable value of ~ 0.3 keV, while the photon index of the tail rises from an initial value of ~ 2.0 to a peak of ~ 3.6.

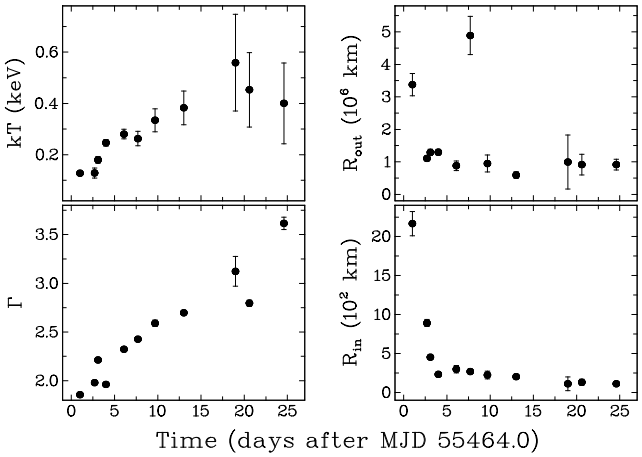

Figure 5. Evolution of the disk temperature (top left), photon index of the Compton tail (bottom left), outer disk radius (top right), and inner disk radius (bottom right). These parameters are based on spectral fits to the broadband SEDs indicated in Figure 1, using the irradiated disk model.

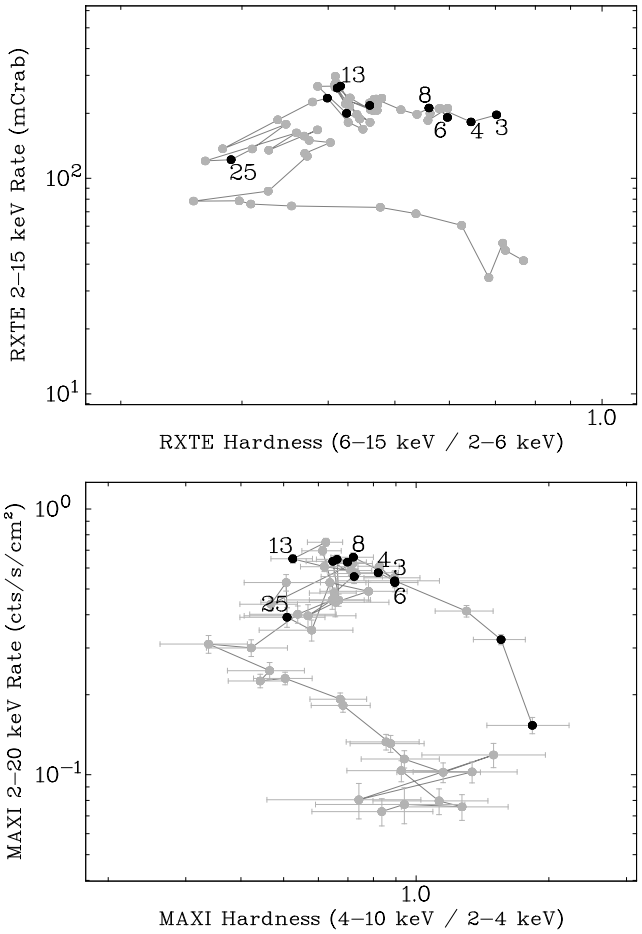

Figure 6. Hardness-intensity diagram for the RXTE (top) and MAXI (bottom; up to MJD 55515) data. The black dots indicate the epochs of X-ray observations for which we have (quasi-) simultaneous radio data. We have indicated the epochs on days 3, 4, 6, 8, 13 and 25 from the radio spectra shown in Figure 2. Note that RXTE was not observing MAXI J1659−152 from the outburst onset, hence there is one less black dot in the top panel compared to the bottom panel.

As the disk temperature rises, the contribution that the Compton tail makes to the disk luminosity, L_C/L_{disk}, decreases, although this is poorly constrained on many epochs, and at late times is consistent with zero. Likewise, the fraction of bolometric flux which is thermalised in the outer disk, F_{out}, decreases although this is also poorly constrained. Since L_C/L_{disk} and F_{out} are poorly constrained, we have not plotted them in Figure 5. The ratio of outer to inner disk radius, r_{out}, increases with time which is due to the fact that the inner disk radius is decreasing. Instead of displaying r_{out} and $Norm$, we show the physical inner radius R_{in} and outer radius R_{out} in Figure 5. The physical radius R_{in} is related to the apparent radius r_{in} of our fit by $R_{in} \approx 1.19 r_{in}$ (see, e.g. Soria 2007). We have determined r_{in} at all the epochs from the fit values of $Norm$, assuming a source distance of 6 kpc (see Section 5) and an inclination of 70°. R_{out} was derived from R_{in} and the ratio r_{out}. In the next section, we will discuss further the trends in the fitted parameters.

4.2 Implications of Spectral Modeling

4.2.1 Radio SEDs & Spectral Breaks

In this paper we present several epochs with broadband radio SEDs. To help place our SED epochs in the overall context of the behavior of the outburst, we indicate them on the HIDs of both the *RXTE* and MAXI data (Figure 6). In this figure we have indicated the X-ray observation epochs for which we performed broadband SED modeling with (quasi-) simultaneous radio data. MAXI J1659−152 was already in the HIMS when the RXTE observations started, but from the MAXI HID we can deduce that the source was transitioning from the hard state to the HIMS during the first radio observations, $1-2$ days after the outburst onset. Our first radio SED with good broadband coverage is at ~ 3 days after the onset of the X-ray outburst. The radio spectral index α, where $F_\nu \propto \nu^\alpha$, is flat or inverted during the first 10 days over more than an order of magnitude in observing frequency, namely from 1.4 to 22 GHz, as one would expect from a synchrotron emitting, partially self-absorbed jet (Fender 2001) and in full agreement with the observed VLBI structure (see Paragi et al. 2013, and the references therein). The spectrum is not constant over that time span though, with an inverted spectrum at day 4 with $\alpha = 0.20 \pm 0.02$, while it is flat at other epochs (see Figure 3). More striking is the sharp spectral break between 22 and 43 GHz that we find on days 6 and 8. After ∼10 days the radio flux drops significantly, but the spectrum is inverted even up to the sub-millimeter bands.

At day 13 the spectrum appears more complicated, with a sharp spectral break above 22 GHz, and a best-fitting spectral index of $\alpha = -0.49 \pm 0.07$ at lower frequencies. We note, however, that the 1.4 and 2.3 GHz WSRT data were taken roughly 8 hours prior to the higher-frequency VLA data used to construct the spectrum shown in Figure 2, and since the source was undergoing a rapid decay, may have overestimated the true low-frequency emission at the time of the VLA observations. Furthermore, any variations from a compact, partially self-absorbed jet will be detected later at

lower frequencies, since the lower-frequency emission comes from further downstream in the jets. Thus, for a rapidly-decaying compact jet, we might expect the lowest-frequency emission to be slightly overestimated, relative to the power law seen at higher frequencies. Combined, these two effects could explain the deviation of the low-frequency spectrum on day ~ 13 from a pure power law. To mitigate against this effect, we refitted the radio spectrum using only the VLA data between 4.9 and 22 GHz, to give a low-frequency spectral index of $\alpha = -0.22 \pm 0.09$, with a break to $\alpha < -2.3$ above 22 GHz.

When the radio flux increases again and the source moves into the SIMS, the spectrum remains flat, but we do not have the spectral coverage at high radio frequencies to check for a spectral break. The radio measurements at day 25 are also consistent with being flat or inverted, but then with a sharp break in between 4.9 and 8.5 GHz.

From the radio light curves in Figure 1 and the spectral index evolution in Figure 3 it appears that the decrease in the radio emission around day 13 after the outburst onset did not coincide with a significant steepening of the spectrum, as observed in other BHXBs (e.g. Kuulkers et al. 1999; Fender, Belloni & Gallo 2004; Miller-Jones et al. 2012). The low-frequency radio emission remained consistent with a partially self-absorbed compact jet throughout the HIMS, with no evidence for ejection events, in agreement with the absence of ejecta in the VLBI images of Paragi et al. (2013).

At higher frequencies, however, the radio spectrum exhibited a high-frequency break above 22 GHz from day ~ 6 until at least day ~ 13, and the optically thin spectrum appeared to steepen with time. This spectral break can be interpreted as the transition from optically thick and partially self-absorbed to optically thin synchrotron emission, and has previously been observed in several other BHXBs in hard X-ray states although usually at much higher frequencies (Russell et al. 2013a). Recently, Russell et al. (2013b) have shown that the BHXB MAXI J1836−194 has an inverted spectrum with a break towards a steep spectrum moving from the mid-infrared to lower frequencies as the source softens in the X-ray regime, and then back to higher frequencies as it gets harder again. With sufficiently dense monitoring over a broad radio frequency range one could be able to see the spectral break pass through the radio bands, which may explain what is happening between days 6 and 13 in MAXI J1659−152 (i.e. the inverse of what was seen during the reverse transition in GX339-4 by Corbel et al. 2013b). There appears to be a relatively rapid increase in the break frequency on day 10, shifting up to > 345 GHz briefly before dropping back to 22 GHz on day 13. Since this is based on a spectrum consisting of flux density measurements at two frequencies, 4.9 and 345 GHz, this break frequency limit is quite uncertain. An inverted spectrum would shift it to a lower value, e.g. with a spectral index of 0.5 the break is at ~ 170 GHz, lower than the limit of 345 GHz but still significantly larger than 22 GHz. Nonetheless, the evolution of the break frequency at that time is fast, but this is not unprecedented: in GX 339-4 the spectral break shifted in the mid-infrared by more than an order of magnitude on timescales of hours when it was in the hard state (Gandhi et al. 2011). Given that the radio-emitting part of the jet is significantly larger than the infrared-emitting region, strong variability on a timescale of days in the case of MAXI J1659−152 could be expected. Alternatively, this could be a short-lived flare at sub-millimeter frequencies. Flares get smoothed out and have reduced amplitude at lower frequencies, which could explain the lack of a flare at 4.9 GHz.

The radio light curve shows an increase in flux between day 17 and 21, while the spectrum remains flat. In Figures 1 and 3 it can been seen that this coincides with a state transition (back and forth between the SIMS and the HIMS), consistent with what has been found for other BHXBs (e.g. Corbel et al. 2013b,a; Russell et al. 2013b). From these observations it seems that the jet started quenching in the HIMS and finished in the SIMS, but then recovered through a second HIMS and peaked in the second SIMS phase, before quenching again after a transition into the soft state. These changes in the radio emission coming from the jet and the X-ray state changes suggest a strong link between the accretion flow and the jet. It also shows that reaching the SIMS is no guarantee of a full transition to a jet ejection event, because there is no major radio flare when the sources moves into the soft state, and no discrete ejecta were detected in the VLBI observations (Paragi et al. 2013). Some other BHXBs in outburst also did not have ejection events, for instance Cyg X−1 (Rushton et al. 2012), but that source did not trace out a canonical track in the HID, while MAXI J1659−152 did (Muñoz-Darias et al. 2011). The soft state in MAXI J1659−152, however, was slightly harder than seen in BHXBs with ejection events, and the minimum fractional variability in the soft state was slightly higher (a minimum of 3%, and rising to 8% when the X-ray emission was softest; Muñoz-Darias et al. 2011). The authors attributed this to the high inclination of the system, but if it was instead intrinsic, the implied difference in the behaviour of the accretion flow could be related to the lack of jet ejection events. Miller-Jones et al. (2012) have shown, however, that the ejection event occurs well before reaching the soft state, at the HIMS/SIMS transition (see also Fender, Homan & Belloni 2009). Since the behaviour of MAXI J1659−152 was relatively standard in the HIMS and SIMS, it seems unlikely that the unusual behaviour in the soft state could be causally related to the lack of ejection events.

4.2.2 Physical Constraints from the Irradiated Disk Model

In Figure 5 we show the evolution of the parameters of the irradiated disk model, in particular the disk temperature, the photon index of the Comptonised tail, and the inner and outer radius of the accretion disk. From this figure we can see that the source is getting spectrally softer (steeper photon index), the disk temperature is increasing, and the inner radius is decreasing, while the outer radius is fairly constant. The latter is not true for the first and sixth epoch, where we have only few nIR/optical data points to constrain the outer radius reliably. Excluding those epochs, the outer radius has a value of $\approx 0.9 - 1.6 \times 10^6$ km, physically realistic considering the orbital separation (Kuulkers et al. 2013) and consistent with the position of the Lagrangian point $> 10^6$ km. The inner radius of the disk is decreasing in time from ~ 890 to ~ 110 km, as one would expect in the standard picture of the disk evolution during a BHXB outburst. From the final value of R_{in} (at day 25 after the outburst

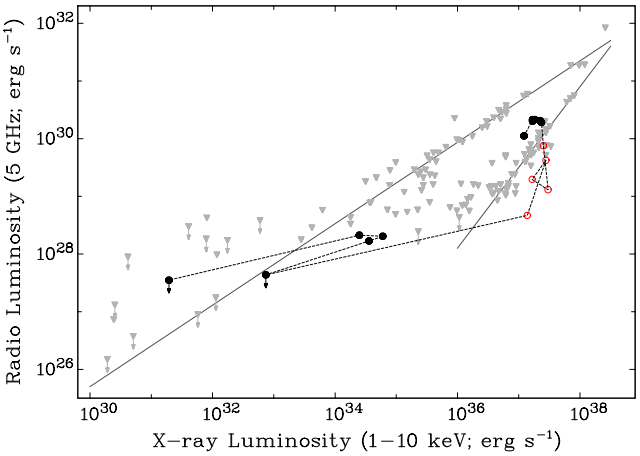

Figure 7. Correlation between the radio and X-ray luminosity during the outburst of MAXI J1659−152, compared to other BHXBs (grey symbols). The grey lines indicate the two tracks in the radio-X-ray correlation with slopes of ~ 0.7 and ~ 1.4. The MAXI J1659−152 luminosities are calculated for a source distance of 6 kpc. The black solid circles indicate the early times of the outburst when the radio emission in MAXI J1659−152 had not dropped significantly yet (up to day 8 after the outburst onset) and the late times when the source is almost in quiescence (> 135 days), while the red open circles indicate the times in between.

onset) we can put an upper limit on the black hole mass by assuming that R_{in} is larger than the innermost stable circular orbit, $R_{ISCO} \equiv 6GM/c^2$ km for a non-rotating, Schwarzschild black hole. The resulting black hole mass of MAXI J1659−152 is $< 12 M_{\odot}$, consistent with the mass derived by Yamaoka et al. (2012). We note that these mass estimates would be larger if the black hole were spinning and they should be treated with caution since they are model-dependent.

5 RADIO-X-RAY & OPTICAL-X-RAY CORRELATIONS

5.1 Radio versus X-rays

In Section 4.1 we have discussed the related behavior between the radio and X-ray regime for MAXI J1659−152, and the implied link between the accretion flow and the jet. We explore this further by investigating the correlation between the radio and X-ray luminosities throughout the outburst. This correlation was originally suggested for GX 339−4 when it was in the hard state (Hannikainen et al. 1998) and described by a power law with index ~ 0.7 extending 3 orders of magnitude in luminosity with a turnover at high X-ray luminosities caused by a quenching of the radio emission in the soft state (Corbel et al. 2003; Gallo, Fender & Pooley 2003). This correlation has not only been found and studied in detail for individual sources (e.g. Corbel, Koerding & Kaaret 2008; Corbel et al. 2013b), but also for the sample of BHXBs as a whole (e.g. Gallo, Fender & Pooley 2003). In recent years a more complex picture has revealed itself, with two distinct tracks in the radio/X-ray luminosity plane (e.g. Coriat et al. 2011; Gallo, Miller & Fender 2012). The second track lies below the first one and has a steeper power-law index of ~ 1.4. For a few sources it has been shown that there is a transition from the lower to the upper track at low luminosities (Coriat et al. 2011; Ratti et al. 2012).

Figure 7 shows the correlation for MAXI J1659−152, and a comparison with other BHXBs in the hard state. Besides the radio observations presented in this paper, we included the late-time data from Jonker et al. (2012). The latter paper focused mainly on the late-time evolution when the source was close to quiescence and also showed the early radio fluxes that had been reported in the literature (van der Horst et al. 2010b; Paragi et al. 2010). To calculate the luminosities we adopted a distance to MAXI J1659−152 of 6 kpc, since the distances estimated in various ways span a range from 4 to 8 kpc (Kennea et al. 2011; Miller-Jones et al. 2011; Kaur et al. 2012; Kuulkers et al. 2013).

As shown by Jonker et al. (2012), MAXI J1659−152 was on the lower track early in the outburst, and once the source had reached quiescent levels, it seemed to transition to the upper track, although we note that the lowest-luminosity points have only radio upper limits. With our extensive data set during the early phases of the outburst we show in Figure 7 that the source gradually evolved off the correlation during the HIMS over the course of several days, as seen before in GX 339-4 (Corbel et al. 2013a) and expected for sources which are not in the hard state. However, the motion in the radio/X-ray plane was not monotonic during this radio quenching, with the radio emission fading and recovering between days 6 and 20, due in part to the repeated transitions between the HIMS and the SIMS.

5.2 Optical versus X-rays

While the radio emission is produced in the jet and the X-ray emission in the accretion disk and/or the corona, the nature of the UV, optical and nIR emission is less unambiguous. Most likely the UV emission is also produced in the accretion disk, either intrinsically or by reprocessing of X-rays, but in the optical and nIR there may also be a contribution from the jet. In Section 4.1 we have modeled the full SED from radio to X-ray frequencies with a combination of a broken power law and a physically motivated irradiated disk model. From these spectral fits we have concluded that a jet contribution at nIR wavelengths is not necessary. This conclusion, however, is model dependent and here we look deeper into this issue by investigating the correlations between the X-ray emission and the nIR, optical and UV emission.

A correlation between the nIR/optical and X-ray luminosity was first found for GX 339−4 in the hard state by Homan et al. (2005), with a power-law slope of ~ 0.5. Russell et al. (2006) has shown for a large sample of BHXBs in the hard state that there is such a correlation with a power-law slope of ~ 0.6 over eight orders of magnitude in X-ray luminosity. A correlation with such a power-law slope can be expected both in the case of X-ray reprocessing (van Paradijs & McClintock 1994) and jet emission at nIR/optical wavelengths. Russell et al. (2006) have also shown that when these sources are in a soft state, the nIR and, in some cases, the optical emission is sig-

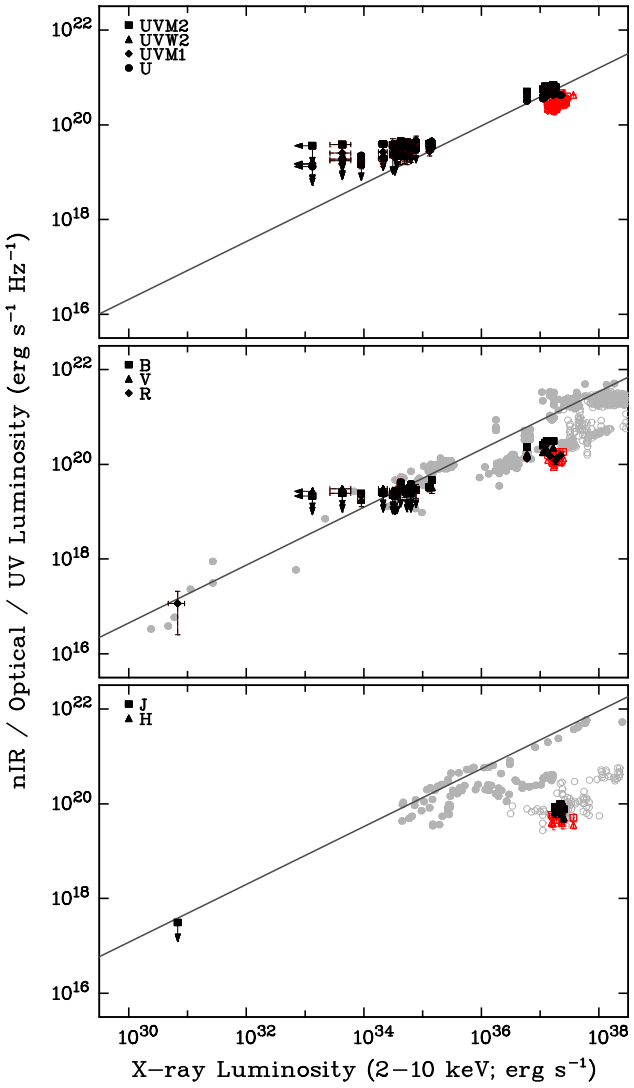

Figure 8. Correlation between the nIR/optical/UV and X-ray luminosity during the outburst of MAXI J1659−152. The MAXI J1659−152 luminosities are calculated for a source distance of 6 kpc. The black solid symbols indicate the early times of the outburst when the radio emission in MAXI J1659−152 had not dropped yet (up to day 8 after the outburst onset) and the late times when the source is almost in or in quiescence (> 135 days), while the red open symbols indicate the times in between. The light grey symbols are for other BHXBs during the hard state (solid symbols) and soft state (open symbols) as presented by Russell et al. (2006) and Russell et al. (2007). The solid lines show the best-fit hard state nIR/optical-X-ray correlation from Russell et al. (2006).

nificantly suppressed. In Figure 8 we show the correlation between the UV/optical/nIR and X-ray luminosities for MAXI J1659−152. Similar to Figure 7 we have made a distinction between the early outburst before the radio emission strongly decreases (day 8 after the outburst onset; black solid symbols), the second phase of the outburst (red open symbols), and the very late times when the source has reached significantly lower luminosities in the radio, optical and X-rays (black solid symbols). We have also included the optical/nIR detections when the source is in quiescence, using the r-band magnitude at $\sim$ 1.5 years after the outburst onset from Kong (2012), the J-band magnitude at $\sim$ 2.9 years from this paper, and the quiescent X-ray flux at $\sim$ 1.8 years reported in Homan et al. (2013). From the late-time magnitudes we have subtracted a contribution from the companion star of the black hole. It has been proposed (Kuulkers et al. 2013; Kong 2012) that this is an M2 or M5 dwarf star, which have an absolute V-band magnitude of 10 and 11.8, respectively (Kong 2012). We have converted these absolute magnitudes to apparent magnitudes in the r- and J-band by correcting for the typical color of these dwarf stars (Johnson 1965) and galactic extinction, and by adopting a source distance of 6 kpc. The resulting r-band magnitude of the companion star is 24.3 (M2) or 25.8 (M5), and in the J-band it is 21.1 (M2) or 22.0 (M5). We have corrected the very-late time fluxes for these ranges in magnitudes, resulting in the large uncertainties displayed in Figure 8.

For comparison we plot in Figure 8 the optical/nIR-X-ray relations for the samples presented in Russell et al. (2006) and Russell et al. (2007), although here we show the luminosity divided by observing frequency for optical/nIR frequencies, i.e. the measured flux scaled by the source distance. For the other BHXBs the solid symbols indicate when they are in a hard state, while the open symbols are for the soft state. The top panel of Figure 8 shows that the UV emission is consistent with the hard state optical-X-ray correlation (Russell et al. 2006) throughout the outburst. In the middle panel it can be seen that MAXI J1659−152 resides in the same region of the correlation as several other hard state BHXBs in the optical, both early in the outburst before the radio emission is quenched and the late times when the source is going towards or is in quiescence. The data corresponding to times after the quenching of the radio emission lay below the correlation of hard state BHXBs, but they are consistent with other sources in the soft state. The bottom panel displays different behavior at nIR wavelengths: the data are well below the correlation for other hard state sources throughout the main outburst (no late-time nIR observations are available), but consistent with some BHXBs in the soft state. This suggests that at the time of our observations there is no significant contribution of the jet to the nIR emission, which is consistent with our conclusions from the broadband modeling in Section 4.1. Given the detection of a spectral break at radio frequencies the lack of nIR jet emission is not surprising. We note, however, that our nIR observations started $\sim$ 4 days after the outburst onset, and our earliest detection of a break was at $\sim$ 6 days, so there is a possibility that the nIR jet emission quenched much earlier than at radio wavelengths. This is consistent with what has been found in other sources, namely that the nIR emission from the jet drops as soon as a source enters the HIMS (e.g. Homan et al. 2005; Coriat et al. 2009; Russell et al. 2010b) while the radio flux quenches later (e.g. Fender, Belloni & Gallo 2004), caused by the jet spectral break shifting to lower frequencies.

6 CONCLUSIONS

In this paper we have presented the results of our observing campaign of MAXI J1659−152 across the electromagnetic spectrum, resulting in one of the richest broadband

data sets of a BHXB outburst with observations at radio, sub-millimeter, nIR, optical, UV and X-ray frequencies, from 1 day up to 3 years after the outburst onset. We have modeled SEDs from radio to X-ray frequencies at several epochs with a broken power law plus a physical irradiated disk model, and we have presented the radio-X-ray and nIR/optical/UV-X-ray correlations for MAXI J1659−152 in the context of other BHXBs.

We have found changes in the radio brightness and spectrum which are correlated with X-ray state changes, suggesting a link between the radio jet and the accretion flow that is dominating the X-ray emission. We have shown this based on our broadband SED modeling and by investigating the correlation between radio and X-ray luminosity. During the first weeks after the outburst onset MAXI J1659−152 moved away from the hard state into intermediate X-ray spectral states, based on spectral and timing behavior at X-ray energies. This was further evidenced by (1) the increasing disk temperature, steepening photon index and decreasing disk inner radius we have found in our SED modeling, (2) the quenching of the radio emission coming from the jet, and (3) the deviations from the radio-X-ray and nIR/optical/UV-X-ray correlations of BHXBs in the hard state.

The broadband radio light curves and spectra support the conclusions from Paragi et al. (2013), based on VLBI observations, that there was no major ejection event. Our radio observations also show the presence of a variable spectral break at radio frequencies during the HIMS and SIMS, significantly lower in frequency than typically found in hard state BHXBs. We have investigated the nIR/optical/UV-X-ray correlations and concluded that there is no significant contribution from the jet at nIR wavelengths, consistent with our broadband modeling. Taken with the results of Russell et al. (2013b) and Corbel et al. (2013a), this suggests that the spectral break, which lies at infrared frequencies during the hard state, evolves down in frequency during the HIMS and SIMS until it passes through the radio band.

Our findings for MAXI J1659−152 demonstrate that broadband observations covering several radio and nIR/optical/UV frequencies at a high cadence during BHXB outbursts are important for a better understanding of the jet and disk in these sources. On top of these observations, denser sampling at sub-millimeter and mid-infrared frequencies are crucial to accurately determine the evolution of the spectral break and further our understanding of the jet physics in these systems.

ACKNOWLEDGMENTS

We greatly appreciate the support from the VLA, WSRT, APEX, ATCA, GMRT, SMARTS, IAC80, 1.23m CAHA, BOOTES-2 and BOOTES-3 telescopes in their help with scheduling and obtaining these observations. The National Radio Astronomy Observatory is operated by Associated Universities, Inc., under cooperative agreement with the National Science Foundation. The WSRT is operated by ASTRON (Netherlands Institute for Radio Astronomy) with support from the Netherlands foundation for Scientific Research. APEX is a collaboration between the Max-Plank-Institut für Radioastronomie, the European Southern Observatory and the Onsala Space Observatory. The ATCA is funded by the Commonwealth of Australia for operation as a National Facility managed by CSIRO. The GMRT is operated by the National Center for Radio Astrophysics of the Tata Institute of Fundamental Research. The CTIO 1.3m telescope is operated by the SMARTS consortium. The Centro Astronómico Hispano Alemán (CAHA) at Calar Alto is operated jointly by the Max-Planck Institut für Astronomie and the Instituto de Astrofísica de Andalucía (CSIC). The Liverpool Telescope is operated on the island of La Palma by Liverpool John Moores University in the Spanish Observatorio del Roque de los Muchachos of the Instituto de Astrofisica de Canarias with financial support from the UK Science and Technology Facilities Council. The IAC80 is operated on the island of Tenerife by the IAC in the Spanish Observatorio del Teide. The MAXI/GSC data are provided by RIKEN, JAXA and the MAXI team. This research has made use of data obtained from the High Energy Astrophysics Science Archive Research Center (HEASARC), provided by NASA's Goddard Space Flight Center.

AJvdH and RAMJW acknowledge support from the European Research Council via Advanced Investigator Grant no. 247295. PAC and JCAMJ acknowledge support from the Australian Research Council's *Discovery Projects* funding scheme under grant DP120102393. DMR acknowledges support from a Marie Curie Intra European Fellowship within the 7th European Community Framework Programme under contract no. IEF 274805. AdUP acknowledges support by the European Commission under the Marie Curie Career Integration Grant programme (FP7-PEOPLE-2012-CIG 322307), and the Dark Cosmology Centre, funded by the DNRF. This work was supported by he Unidad Asociada IAA-CSIC at the group of planetary science of ETSI-UPV/EHU, by the Ikerbasque Foundation for Science, and by Spanish research programs AYA2012-39362-C02-02, AYA2011-24780/ESP, AYA2009-14000-C03-01/ESP and AYA2010-21887-C04-01. TB acknowledges support from grant PRIN-INAF 2012. RW acknowledges support from the European Research Council via a Starting Grant.

REFERENCES

Belloni T., ed., 2010, Lecture Notes in Physics, Berlin Springer Verlag, Vol. 794, The Jet Paradigm
Belloni T. M., Motta S., Muñoz-Darias T., 2010, The Astronomer's Telegram, 2927, 1
Belloni T. M., Muñoz-Darias T., Kuulkers E., 2010, The Astronomer's Telegram, 2926, 1
Breeveld A. A. et al., 2010, MNRAS, 406, 1687
Casella P., Belloni T., Stella L., 2005, ApJ, 629, 403
Castro-Tirado A. J. et al., 1999, A&AS, 138, 583
Corbel S. et al., 2013a, MNRAS, 431, L107
Corbel S., Coriat M., Brocksopp C., Tzioumis A. K., Fender R. P., Tomsick J. A., Buxton M. M., Bailyn C. D., 2013b, MNRAS, 428, 2500
Corbel S., Fender R. P., 2002, ApJ, 573, L35
Corbel S., Koerding E., Kaaret P., 2008, MNRAS, 389, 1697
Corbel S., Nowak M. A., Fender R. P., Tzioumis A. K., Markoff S., 2003, A&A, 400, 1007
Coriat M., Corbel S., Buxton M. M., Bailyn C. D., Tomsick J. A., Körding E., Kalemci E., 2009, MNRAS, 400, 123

Coriat M. et al., 2011, MNRAS, 414, 677
de Ugarte Postigo A., Flores H., Wiersema K., Thoene C. C., Fynbo J. P. U., Goldoni P., 2010a, GRB Coordinates Network, Circular Service, 11307, 1 (2010), 1307, 1
de Ugarte Postigo A., Lundrgren A., Wyrowski F., Thoene C. C., Castro-Tirado A. J., Gorosabel J., Jelinek M., 2010b, GRB Coordinates Network, Circular Service, 11304, 1 (2010), 1304, 1
Evans P. A. et al., 2009, MNRAS, 397, 1177
Fender R., 2010, in Lecture Notes in Physics, Berlin Springer Verlag, Vol. 794, Lecture Notes in Physics, Berlin Springer Verlag, Belloni T., ed., p. 115
Fender R. P., 2001, MNRAS, 322, 31
Fender R. P., Belloni T. M., Gallo E., 2004, MNRAS, 355, 1105
Fender R. P., Homan J., Belloni T. M., 2009, MNRAS, 396, 1370
Fukugita M., Ichikawa T., Gunn J. E., Doi M., Shimasaku K., Schneider D. P., 1996, AJ, 111, 1748
Fukugita M., Shimasaku K., Ichikawa T., 1995, PASP, 107, 945
Gallo E., 2010, in Lecture Notes in Physics, Berlin Springer Verlag, Vol. 794, Lecture Notes in Physics, Berlin Springer Verlag, Belloni T., ed., p. 85
Gallo E., Fender R. P., Pooley G. G., 2003, MNRAS, 344, 60
Gallo E., Miller B. P., Fender R., 2012, MNRAS, 423, 590
Gandhi P. et al., 2011, ApJ, 740, L13
Gierliński M., Done C., Page K., 2008, MNRAS, 388, 753
Gierliński M., Done C., Page K., 2009, MNRAS, 392, 1106
Gilfanov M., 2010, in Lecture Notes in Physics, Berlin Springer Verlag, Vol. 794, Lecture Notes in Physics, Berlin Springer Verlag, Belloni T., ed., p. 17
Hannikainen D. C., Hunstead R. W., Campbell-Wilson D., Sood R. K., 1998, A&A, 337, 460
Homan J., Belloni T., 2005, Ap&SS, 300, 107
Homan J., Buxton M., Markoff S., Bailyn C. D., Nespoli E., Belloni T., 2005, ApJ, 624, 295
Homan J., Fridriksson J. K., Jonker P. G., Russell D. M., Gallo E., Kuulkers E., Rea N., Altamirano D., 2013, ArXiv e-prints
Homan J., Wijnands R., van der Klis M., Belloni T., van Paradijs J., Klein-Wolt M., Fender R., Méndez M., 2001, ApJS, 132, 377
Jelinek M. et al., 2010, GRB Coordinates Network, Circular Service, 11301, 1 (2010), 1301, 1
Johnson H. L., 1965, ApJ, 141, 170
Jonker P. G., Miller-Jones J. C. A., Homan J., Tomsick J., Fender R. P., Kaaret P., Markoff S., Gallo E., 2012, MNRAS, 423, 3308
Jordi K., Grebel E. K., Ammon K., 2006, A&A, 460, 339
Kalamkar M., Homan J., Altamirano D., van der Klis M., Casella P., Linares M., 2011, ApJ, 731, L2
Kalamkar M. et al., 2010, The Astronomer's Telegram, 2881, 1
Kalberla P. M. W., Burton W. B., Hartmann D., Arnal E. M., Bajaja E., Morras R., Pöppel W. G. L., 2005, A&A, 440, 775
Kann D. A., 2010, GRB Coordinates Network, Circular Service, 11299, 1 (2010), 1299, 1
Kaur R. et al., 2012, ApJ, 746, L23
Kennea J. A., Krimm H., Mangano V., Curran P., Romano P., Evans P., Burrows D. N., 2010, The Astronomer's Telegram, 2877, 1
Kennea J. A. et al., 2011, ApJ, 736, 22
Kong A. K. H., 2012, ApJ, 760, L27
Kuulkers E., Fender R. P., Spencer R. E., Davis R. J., Morison I., 1999, MNRAS, 306, 919
Kuulkers E. et al., 2010, The Astronomer's Telegram, 2912, 1
Kuulkers E. et al., 2013, A&A, 552, A32
Kuulkers E. et al., 2012, in The First Year of MAXI: Monitoring variable X-ray sources – 4th International MAXI Workshop, Mihara T. & Serino M., ed., Vol. IPCR CR-127, 81
Lundgren A. et al., 2010, in Society of Photo-Optical Instrumentation Engineers (SPIE) Conference Series, Vol. 7737, Society of Photo-Optical Instrumentation Engineers (SPIE) Conference Series
Malzac J., Dumont A. M., Mouchet M., 2005, A&A, 430, 761
Mangano V., Hoversten E. A., Markwardt C. B., Sbarufatti B., Starling R. L. C., Ukwatta T. N., 2010, GRB Coordinates Network, Circular Service, 11296, 1 (2010), 1296, 1
Markoff S., Nowak M. A., 2004, ApJ, 609, 972
Marshall F. E., 2010, GRB Coordinates Network, Circular Service, 11298, 1 (2010), 1298, 1
McClintock J. E., Remillard R. A., 2006, Black hole binaries, Lewin W. H. G., van der Klis M., eds., pp. 157–213
Miller J. M., Homan J., Miniutti G., 2006, ApJ, 652, L113
Miller-Jones J. C. A., Madej O. K., Jonker P. G., Homan J., Ratti E. M., Torres M. A. P., 2011, The Astronomer's Telegram, 3358, 1
Miller-Jones J. C. A. et al., 2012, MNRAS, 421, 468
Mirabel I. F., Rodriguez L. F., Cordier B., Paul J., Lebrun F., 1992, Nature, 358, 215
Monet D. G. et al., 2003, AJ, 125, 984
Motta S., Muñoz-Darias T., Casella P., Belloni T., Homan J., 2011, MNRAS, 418, 2292
Muñoz-Darias T., Motta S., Stiele H., Belloni T. M., 2011, MNRAS, 415, 292
Muñoz-Darias T., Stiele H., Belloni T. M., Motta S., 2010, The Astronomer's Telegram, 2999, 1
Negoro H. et al., 2010, The Astronomer's Telegram, 2873, 1
Paragi Z. et al., 2013, MNRAS, 432, 1319
Paragi Z. et al., 2010, The Astronomer's Telegram, 2906, 1
Poole T. S. et al., 2008, MNRAS, 383, 627
Ratti E. M. et al., 2012, MNRAS, 423, 2656
Rushton A. et al., 2012, MNRAS, 419, 3194
Russell D. M., Fender R. P., Hynes R. I., Brocksopp C., Homan J., Jonker P. G., Buxton M. M., 2006, MNRAS, 371, 1334
Russell D. M. et al., 2010a, The Astronomer's Telegram, 2884, 1
Russell D. M., Maccarone T. J., Körding E. G., Homan J., 2007, MNRAS, 379, 1401
Russell D. M., Maitra D., Dunn R. J. H., Markoff S., 2010b, MNRAS, 405, 1759
Russell D. M. et al., 2013a, MNRAS, 429, 815
Russell D. M. et al., 2013b, ApJ, 768, L35

Rykoff E. S., Miller J. M., Steeghs D., Torres M. A. P., 2007, ApJ, 666, 1129
Sault R. J., Teuben P. J., Wright M. C. H., 1995, in Astronomical Society of the Pacific Conference Series, Vol. 77, Astronomical Data Analysis Software and Systems IV, Shaw R. A., Payne H. E., Hayes J. J. E., eds., p. 433
Schlegel D. J., Finkbeiner D. P., Davis M., 1998, ApJ, 500, 525
Shakura N. I., Sunyaev R. A., 1973, A&A, 24, 337
Shaposhnikov N., Yamaoka K., 2010, The Astronomer's Telegram, 2951, 1
Siringo G. et al., 2009, A&A, 497, 945
Skrutskie M. F. et al., 1995, in Bulletin of the American Astronomical Society, Vol. 27, American Astronomical Society Meeting Abstracts, p. 1392
Soria R., 2007, Ap&SS, 311, 213
Subasavage J. P., Bailyn C. D., Smith R. C., Henry T. J., Walter F. M., Buxton M. M., 2010, in Society of Photo-Optical Instrumentation Engineers (SPIE) Conference Series, Vol. 7737, Society of Photo-Optical Instrumentation Engineers (SPIE) Conference Series
Tan G. H., 1991, in Astronomical Society of the Pacific Conference Series, Vol. 19, IAU Colloq. 131: Radio Interferometry. Theory, Techniques, and Applications, Cornwell T. J., Perley R. A., eds., pp. 42–46
van der Horst A. J., Granot J., Paragi Z., Kouveliotou C., Wijers R. A. M. J., Ramirez-Ruiz E., 2010a, GRB Coordinates Network, Circular Service, 11309, 1 (2010), 1309, 1
van der Horst A. J., Granot J., Paragi Z., Kouveliotou C., Wijers R. A. M. J., Ramirez-Ruiz E., 2010b, The Astronomer's Telegram, 2874, 1
van der Horst A. J. et al., 2010c, The Astronomer's Telegram, 2918, 1
van Paradijs J., McClintock J. E., 1994, A&A, 290, 133
Wells D. C., 1985, in Data Analysis in Astronomy, di Gesu V., Scarsi L., Crane P., Friedman J. H., Levialdi S., eds., p. 195
Wijnands R., Homan J., van der Klis M., 1999, ApJ, 526, L33
Wilson W. E. et al., 2011, MNRAS, 416, 832
Xu D., 2010, GRB Coordinates Network, Circular Service, 11303, 1 (2010), 1303, 1
Yamaoka K. et al., 2012, PASJ, 64, 32

Table 2. UV, optical and nIR observations

Epoch (MJD)	Telescope	Filter	Magnitude
55468.050	SMARTS	H	14.70±0.13
55468.995	SMARTS	H	14.85±0.12
55469.999	SMARTS	H	14.88±0.21
55470.990	SMARTS	H	14.90±0.18
55472.002	SMARTS	H	15.02±0.08
55472.985	SMARTS	H	15.22±0.15
55476.002	SMARTS	H	15.33±0.14
55476.994	SMARTS	H	15.60±0.14
55478.010	SMARTS	H	15.40±0.14
55478.997	SMARTS	H	15.50±0.18
55479.997	SMARTS	H	15.49±0.14
55481.006	SMARTS	H	15.54±0.24
55483.002	SMARTS	H	15.51±0.21
55468.044	SMARTS	J	15.13±0.13
55468.990	SMARTS	J	15.27±0.19
55469.993	SMARTS	J	15.26±0.10
55470.984	SMARTS	J	15.32±0.21
55471.996	SMARTS	J	15.26±0.16
55472.979	SMARTS	J	15.41±0.23
55475.996	SMARTS	J	15.52±0.11
55476.988	SMARTS	J	15.84±0.21
55478.004	SMARTS	J	15.68±0.11
55478.991	SMARTS	J	15.76±0.10
55479.991	SMARTS	J	15.70±0.10
55481.001	SMARTS	J	15.83±0.10
55482.997	SMARTS	J	15.79±0.06
56497.977	3.5m CAHA	J	21.05±0.17
55710.964	2.2m CAHA	z	18.45±0.10
55464.836	IAC80	I	16.09±0.05
55486.768	1.23m CAHA	I	16.59±0.08
55641.198	1.23m CAHA	I	17.95±0.23
55685.141	2.0m LT	i	19.87±0.05
55708.960	2.2m CAHA	i	18.72±0.05
55709.981	2.2m CAHA	i	18.77±0.09
55710.041	2.2m CAHA	i	18.59±0.15
55710.958	2.2m CAHA	i	18.79±0.06
55464.826	IAC80	R	16.59±0.06
55464.834	IAC80	R	16.61±0.05
55464.838	BOOTES-2	R	16.59±0.09
55464.838	IAC80	R	16.58±0.06
55464.839	IAC80	R	16.62±0.05
55464.840	IAC80	R	16.59±0.06
55464.840	IAC80	R	16.56±0.06
55464.841	IAC80	R	16.58±0.06
55464.841	IAC80	R	16.56±0.06
55464.842	IAC80	R	16.59±0.06
55464.842	IAC80	R	16.57±0.06
55464.843	IAC80	R	16.55±0.06
55464.843	IAC80	R	16.56±0.07
55464.846	IAC80	R	16.57±0.07
55464.849	IAC80	R	16.54±0.07
55466.799	BOOTES-2	R	16.45±0.07
55468.798	BOOTES-2	R	16.41±0.06
55469.790	BOOTES-2	R	16.59±0.06
55641.195	1.23m CAHA	R	18.57±0.21
55470.793	BOOTES-2	r	16.69±0.20
55474.358	BOOTES-3	r	16.78±0.11

Table 2 – *continued* UV, optical and nIR observations

Epoch (MJD)	Telescope	Filter	Magnitude
55474.383	BOOTES-3	r	16.74±0.11
55475.314	BOOTES-3	r	17.01±0.11
55475.336	BOOTES-3	r	17.02±0.11
55475.357	BOOTES-3	r	16.98±0.11
55475.378	BOOTES-3	r	16.95±0.11
55475.399	BOOTES-3	r	16.84±0.11
55708.960	2.2m CAHA	r	19.03±0.04
55709.981	2.2m CAHA	r	19.09±0.04
55710.041	2.2m CAHA	r	19.15±0.12
55710.961	2.2m CAHA	r	19.05±0.05
55464.627	UVOT	V	16.775±0.032
55464.832	IAC80	V	16.94±0.03
55465.258	UVOT	V	16.676±0.032
55465.735	UVOT	V	16.571±0.038
55466.303	UVOT	V	16.525±0.031
55467.635	UVOT	V	16.450±0.036
55482.813	UVOT	V	17.197±0.083
55483.489	UVOT	V	17.171±0.067
55484.025	UVOT	V	17.211±0.080
55485.028	UVOT	V	16.974±0.068
55486.031	UVOT	V	17.046±0.068
55487.036	UVOT	V	17.441±0.096
55488.040	UVOT	V	17.178±0.079
55489.044	UVOT	V	17.082±0.075
55490.042	UVOT	V	17.337±0.107
55491.045	UVOT	V	17.258±0.092
55598.791	UVOT	V	18.576±0.284
55620.663	UVOT	V	>18.588
55634.878	UVOT	V	18.756±0.303
55641.195	1.23m CAHA	V	18.67±0.21
55647.369	UVOT	V	>18.963
55669.437	UVOT	V	>18.798
55687.980	UVOT	V	19.253±0.298
55702.627	UVOT	V	18.562±0.214
55717.735	UVOT	V	>18.662
55721.224	UVOT	V	>18.642
55725.361	UVOT	V	>18.661
55729.780	UVOT	V	>18.622
55733.057	UVOT	V	>18.625
55737.405	UVOT	V	>18.788
55741.027	UVOT	V	>18.745
55745.765	UVOT	V	>18.648
55749.584	UVOT	V	>18.658
55757.421	UVOT	V	>18.610
55759.752	UVOT	V	>18.554
55761.296	UVOT	V	>18.344
55470.793	BOOTES-2	g	17.31±0.15
55476.785	BOOTES-2	g	17.42±0.17
55708.960	2.2m CAHA	g	19.60±0.07
55709.981	2.2m CAHA	g	19.66±0.05
55710.041	2.2m CAHA	g	19.81±0.19
55710.961	2.2m CAHA	g	19.62±0.07
55464.666	UVOT	B	17.114±0.023
55464.830	IAC80	B	17.38±0.07
55465.334	UVOT	B	17.014±0.026
55465.727	UVOT	B	16.883±0.028
55466.291	UVOT	B	16.818±0.023

Table 2 – *continued* UV, optical and nIR observations

Epoch (MJD)	Telescope	Filter	Magnitude
55466.628	UVOT	B	16.804±0.030
55467.629	UVOT	B	16.795±0.027
55482.823	UVOT	B	17.378±0.046
55483.502	UVOT	B	17.529±0.045
55484.035	UVOT	B	17.482±0.049
55485.038	UVOT	B	17.366±0.046
55486.042	UVOT	B	17.460±0.048
55487.046	UVOT	B	17.761±0.061
55488.050	UVOT	B	17.483±0.050
55489.054	UVOT	B	17.538±0.053
55490.050	UVOT	B	17.769±0.072
55491.055	UVOT	B	17.613±0.059
55598.851	UVOT	B	18.908±0.128
55620.657	UVOT	B	19.183±0.288
55634.872	UVOT	B	19.434±0.240
55641.198	1.23m CAHA	B	19.71±0.48
55647.363	UVOT	B	19.507±0.252
55669.431	UVOT	B	>19.745
55687.975	UVOT	B	19.624±0.177
55702.620	UVOT	B	19.281±0.176
55717.730	UVOT	B	>19.600
55721.219	UVOT	B	19.440±0.342
55725.356	UVOT	B	>19.607
55729.775	UVOT	B	19.073±0.256
55733.052	UVOT	B	>19.585
55737.399	UVOT	B	>19.738
55741.021	UVOT	B	>19.702
55745.760	UVOT	B	>19.605
55749.579	UVOT	B	>19.595
55757.483	UVOT	B	>19.963
55759.748	UVOT	B	>19.512
55761.428	UVOT	B	>19.893
55464.662	UVOT	U	16.144±0.025
55465.267	UVOT	U	16.036±0.025
55465.725	UVOT	U	15.905±0.028
55466.288	UVOT	U	15.845±0.025
55466.625	UVOT	U	15.787±0.059
55467.628	UVOT	U	15.816±0.027
55468.494	UVOT	U	15.840±0.025
55482.819	UVOT	U	16.450±0.037
55483.496	UVOT	U	16.468±0.034
55484.030	UVOT	U	16.565±0.039
55485.033	UVOT	U	16.382±0.036
55486.037	UVOT	U	16.510±0.037
55487.041	UVOT	U	16.698±0.041
55488.046	UVOT	U	16.550±0.039
55489.049	UVOT	U	16.591±0.040
55490.046	UVOT	U	16.725±0.047
55491.050	UVOT	U	16.678±0.042
55598.850	UVOT	U	18.624±0.132
55620.656	UVOT	U	18.498±0.215
55634.871	UVOT	U	18.469±0.146
55647.362	UVOT	U	19.112±0.244
55669.629	UVOT	U	>19.660
55687.974	UVOT	U	19.078±0.151
55702.619	UVOT	U	18.715±0.149
55717.729	UVOT	U	18.770±0.265

Table 2 – *continued* UV, optical and nIR observations

Epoch (MJD)	Telescope	Filter	Magnitude
55721.218	UVOT	U	18.762±0.268
55725.355	UVOT	U	18.685±0.242
55729.774	UVOT	U	19.125±0.356
55733.051	UVOT	U	19.132±0.351
55737.397	UVOT	U	18.896±0.263
55741.020	UVOT	U	18.591±0.216
55745.759	UVOT	U	19.184±0.375
55749.578	UVOT	U	>19.275
55757.482	UVOT	U	>19.635
55759.747	UVOT	U	>19.202
55761.427	UVOT	U	>19.567
55708.960	2.2m CAHA	u	19.81±0.05
55709.981	2.2m CAHA	u	19.83±0.07
55710.041	2.2m CAHA	u	19.66±0.17
55710.961	2.2m CAHA	u	20.04±0.28
55464.656	UVOT	UVW1	16.438±0.024
55465.260	UVOT	UVW1	16.307±0.024
55465.723	UVOT	UVW1	16.196±0.027
55466.284	UVOT	UVW1	16.117±0.024
55467.626	UVOT	UVW1	16.103±0.026
55471.384	UVOT	UVW1	16.240±0.025
55472.120	UVOT	UVW1	16.317±0.027
55475.400	UVOT	UVW1	16.505±0.025
55476.128	UVOT	UVW1	16.483±0.029
55476.664	UVOT	UVW1	16.528±0.029
55479.073	UVOT	UVW1	16.697±0.035
55479.541	UVOT	UVW1	16.723±0.031
55482.891	UVOT	UVW1	16.639±0.047
55484.576	UVOT	UVW1	16.848±0.052
55485.505	UVOT	UVW1	16.823±0.053
55488.578	UVOT	UVW1	16.765±0.054
55489.527	UVOT	UVW1	16.993±0.063
55490.586	UVOT	UVW1	17.112±0.070
55491.257	UVOT	UVW1	17.165±0.071
55598.848	UVOT	UVW1	18.844±0.120
55620.654	UVOT	UVW1	19.022±0.257
55634.869	UVOT	UVW1	19.459±0.251
55647.361	UVOT	UVW1	19.150±0.208
55669.628	UVOT	UVW1	>20.034
55687.973	UVOT	UVW1	19.722±0.204
55702.616	UVOT	UVW1	19.395±0.211
55717.727	UVOT	UVW1	19.349±0.341
55721.216	UVOT	UVW1	18.815±0.235
55725.353	UVOT	UVW1	19.126±0.284
55729.773	UVOT	UVW1	19.286±0.325
55733.050	UVOT	UVW1	19.360±0.353
55737.396	UVOT	UVW1	>19.658
55741.019	UVOT	UVW1	>19.614
55745.758	UVOT	UVW1	>19.419
55749.577	UVOT	UVW1	>19.490
55757.481	UVOT	UVW1	>19.905
55759.746	UVOT	UVW1	>19.412
55761.426	UVOT	UVW1	>19.846
55464.623	UVOT	UVW2	16.548±0.028
55465.324	UVOT	UVW2	16.470±0.028
55465.732	UVOT	UVW2	16.326±0.025
55466.297	UVOT	UVW2	16.251±0.023

Table 2 – *continued* UV, optical and nIR observations

Epoch (MJD)	Telescope	Filter	Magnitude
55467.632	UVOT	UVW2	16.245±0.024
55469.478	UVOT	UVW2	16.399±0.026
55473.392	UVOT	UVW2	16.506±0.025
55477.132	UVOT	UVW2	16.602±0.030
55477.668	UVOT	UVW2	16.819±0.031
55482.880	UVOT	UVW2	16.853±0.050
55484.565	UVOT	UVW2	17.014±0.052
55485.494	UVOT	UVW2	17.094±0.055
55488.569	UVOT	UVW2	17.111±0.057
55489.519	UVOT	UVW2	17.095±0.060
55490.579	UVOT	UVW2	17.366±0.072
55491.249	UVOT	UVW2	17.348±0.069
55598.852	UVOT	UVW2	19.249±0.100
55620.660	UVOT	UVW2	19.859±0.302
55634.875	UVOT	UVW2	19.889±0.214
55647.366	UVOT	UVW2	19.751±0.201
55669.434	UVOT	UVW2	>20.301
55687.977	UVOT	UVW2	20.305±0.201
55702.624	UVOT	UVW2	19.505±0.143
55717.732	UVOT	UVW2	19.880±0.310
55721.222	UVOT	UVW2	19.441±0.231
55725.358	UVOT	UVW2	19.291±0.201
55729.778	UVOT	UVW2	19.463±0.232
55733.055	UVOT	UVW2	19.332±0.216
55737.402	UVOT	UVW2	19.624±0.235
55741.024	UVOT	UVW2	19.672±0.250
55745.763	UVOT	UVW2	19.993±0.344
55749.582	UVOT	UVW2	>20.115
55757.484	UVOT	UVW2	>20.230
55759.750	UVOT	UVW2	>20.005
55761.430	UVOT	UVW2	>20.298
55464.633	UVOT	UVM2	16.950±0.033
55465.250	UVOT	UVM2	16.835±0.029
55465.739	UVOT	UVM2	16.687±0.032
55466.270	UVOT	UVM2	16.683±0.033
55467.638	UVOT	UVM2	16.602±0.032
55470.481	UVOT	UVM2	16.702±0.031
55474.362	UVOT	UVM2	17.023±0.032
55478.136	UVOT	UVM2	17.174±0.042
55478.671	UVOT	UVM2	17.202±0.042
55482.886	UVOT	UVM2	17.228±0.072
55484.571	UVOT	UVM2	17.435±0.077
55485.500	UVOT	UVM2	17.519±0.082
55488.574	UVOT	UVM2	17.511±0.084
55489.523	UVOT	UVM2	17.451±0.087
55490.583	UVOT	UVM2	17.760±0.107
55491.253	UVOT	UVM2	17.674±0.100
55598.794	UVOT	UVM2	19.738±0.296
55620.666	UVOT	UVM2	>19.757
55634.880	UVOT	UVM2	20.274±0.374
55647.370	UVOT	UVM2	>20.039
55669.440	UVOT	UVM2	>19.817
55687.982	UVOT	UVM2	>20.656
55702.630	UVOT	UVM2	19.713±0.240
55717.737	UVOT	UVM2	>19.584
55721.226	UVOT	UVM2	>19.728
55725.363	UVOT	UVM2	>19.763

Table 2 – *continued* UV, optical and nIR observations

Epoch (MJD)	Telescope	Filter	Magnitude
55729.782	UVOT	UVM2	>19.587
55733.059	UVOT	UVM2	>19.648
55737.407	UVOT	UVM2	>19.720
55741.029	UVOT	UVM2	19.780±0.369
55745.767	UVOT	UVM2	>19.724
55749.586	UVOT	UVM2	>19.752
55757.423	UVOT	UVM2	>19.720
55759.754	UVOT	UVM2	>19.625
55761.298	UVOT	UVM2	>19.405